Atomic-Scale Metal–Insulator Transition in SrRuO₃ Ultrathin Films Triggered by Surface Termination Conversion

Han Gyeol Lee, Lingfei Wang,* Liang Si, Xiaoyue He, Daniel G. Porter, Jeong Rae Kim, Eun Kyo Ko, Jinkwon Kim, Sung Min Park, Bongju Kim, Andrew Thye Shen Wee, Alessandro Bombardi, Zhicheng Zhong, and Tae Won Noh*

The metal–insulator transition (MIT) in transition-metal-oxide is fertile ground for exploring intriguing physics and potential device applications. Here, an atomic-scale MIT triggered by surface termination conversion in SrRuO₃ ultrathin films is reported. Uniform and effective termination engineering at the SrRuO₃(001) surface can be realized via a self-limiting water-leaching process. As the surface termination converts from SrO to RuO₂, a highly insulating and nonferromagnetic phase emerges within the topmost SrRuO₃ monolayer. Such a spatially confined MIT is corroborated by systematic characterizations on electrical transport, magnetism, and scanning tunneling spectroscopy. Density functional theory calculations and X-ray linear dichroism further suggest that the surface termination conversion breaks the local octahedral symmetry of the crystal field. The resultant modulation in 4d orbital occupancy stabilizes a nonferromagnetic insulating surface state. This work introduces a new paradigm to stimulate and tune exotic functionalities of oxide heterostructures with atomic precision.

The metal–insulator transition (MIT), characterized by a dramatic decrease in electrical conductivity, has been widely observed and intensively studied in condensed-matter systems.[1,2] Especially in transition-metal-oxides (TMOs), interplay between lattice, charge, spin, and orbital degrees of freedom enables a diverse array of intriguing MIT phenomena.[3–5] For utilizing these MIT phenomena in practical nanodevices with a high integration level, it is essential to spatially confine the MIT in designed regimes in solids.[6,7] A prominent example of this is ABO_3 perovskite oxide-based epitaxial heterostructures, in which MIT can be easily confined within surfaces, domain walls, and predesigned nanoscale patterns.[8–11] Moreover, metallicity in TMO-based epitaxial systems is typically correlated with other properties like ferroic ordering, optical absorption, and thermal conductivity.[2–4,12] Therefore, harnessing the spatially confined MIT could enable effective control and integration of various functionalities for high-performance logic/memory device applications.

Herein, we present an experimental realization of spatially confined MIT through surface termination conversion. ABO_3 perovskite oxide consists of AO and BO_2 atomic layers alternately stacked along the pseudocubic [001] direction. In a simplified picture, the surface of perovskite oxide should show either AO or BO_2 terminations. At the AO-terminated (001) surface, or in bulk, the crystal field from BO_6 octahedron split d band into t_{2g} and e_g sub-bands.[13] For metallic systems, one of the sub-bands should be partially filled (**Figure 1**a). By contrast, at the BO_2-terminated (001) surface, the loss of apex oxygen may further split the t_{2g} and e_g sub-bands and result

H. G. Lee, Prof. L. Wang, J. R. Kim, E. K. Ko, J. Kim, Dr. S. M. Park, Dr. B. Kim, Prof. T. W. Noh
Center for Correlated Electron Systems
Institute for Basic Science (IBS)
Seoul 08826, Republic of Korea
E-mail: lingfei.wang@outlook.com; twnoh@snu.ac.kr
H. G. Lee, Prof. L. Wang, J. R. Kim, E. K. Ko, J. Kim, Dr. S. M. Park, Dr. B. Kim, Prof. T. W. Noh
Department of Physics and Astronomy
Seoul National University
Seoul 08826, Republic of Korea
Dr. L. Si, Prof. Z. Zhong
Key Laboratory of Magnetic Materials and Devices & Zhejiang Province
Key Laboratory of Magnetic Materials and Application Technology
Ningbo Institute of Materials Technology and Engineering
Chinese Academy of Sciences
Ningbo 315201, P. R. China

Dr. L. Si
Institut für Festkörperphysik
Vienna 1040, Austria
Dr. X. He, Prof. A. T. S. Wee
Department of Physics
National University of Singapore
Singapore 117542, Singapore
Dr. X. He
Songshan Lake Materials Laboratory
Dongguan 523808, P. R. China
Dr. D. G. Porter, Dr. A. Bombardi
Diamond Light Source Ltd.
Harwell Science and Innovation Campus
Didcot, Oxfordshire OX11 0DE, UK
Prof. Z. Zhong
China Center of Materials Science and Optoelectronics Engineering
University of Chinese Academy of Sciences
Beijing 100049, P. R. China

**ADVANCED
SCIENCE NEWS**

www.advancedsciencenews.com
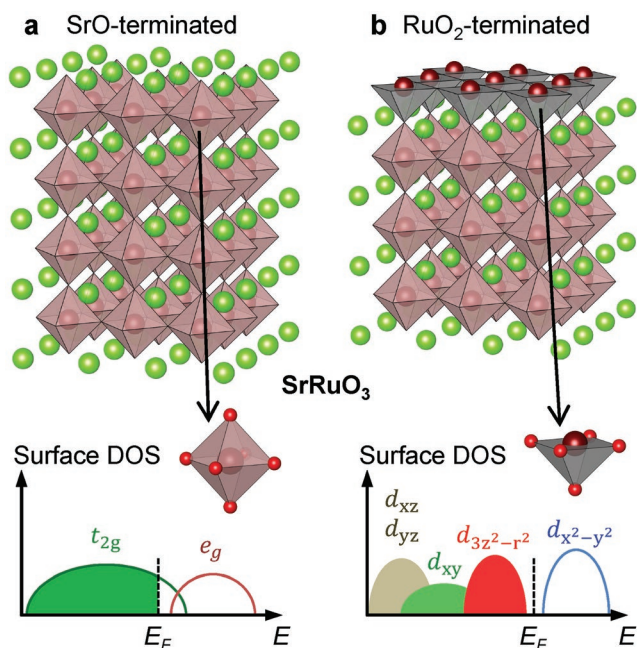
**ADVANCED
MATERIALS**

www.advmat.de

Figure 1. Schematics of termination engineering in SrRuO$_3$ (SRO) films. a) At SrO-terminated SRO film surface and bulk, RuO$_6$ octahedral crystal field split the Ru 4d band into t_{2g} and e_g sub-bands. The partially filled t_{2g} band results in finite density-of-states (DOS) near the Fermi level (E_F), signifying robust metallicity. b) At the RuO$_2$-terminated SRO film surface, on the contrary, the loss of apex oxygen breaks the RuO$_6$ octahedral symmetry. It further splits the t_{2g} and e_g bands. This surface layer becomes highly insulating, featured by a gap-opening in the DOS profile.

in the opening of a gap (Figure 1b). On the basis of these two termination configurations, complicated reconstructions can also occur, which provide additional degrees of freedom to further modify the electronic structure of perovskite oxide surfaces.[14,15] Moreover, such electronic modulations could be highly localized in surface atomic layers.[9,16,17] Accordingly, surface termination engineering could be an effective approach for inducing atomic-scale surface MIT in TMO heterostructures.

We take the SrRuO$_3$ (SRO) ultrathin film as a model system for this study. SRO epitaxial film has been widely used as an electrode layer due to its high electrical conductivity and structural stability.[16,18,19] Furthermore, a fine balance between electron–electron correlation and spin–orbit coupling in SRO gives rise to a variety of intriguing physical phenomena, such as itinerant ferromagnetism,[20,21] magnetic monopoles in momentum space,[22] tunable magnetic skyrmions and, the topological Hall effect.[23,24] Notably, all of these are strongly coupled with metallicity. A spatially confined MIT, if realized through surface termination engineering, can be a powerful tool for locally modulating these exotic phenomena. However, as-grown SRO(001) film surfaces always show SrO termination due to the poor thermodynamic stability of RuO$_2$ termination.[25]

Here, we developed an ex situ water-leaching recipe and achieved self-limiting surface termination engineering at room temperature. We found that the RuO$_2$-terminated SRO surface monolayer becomes highly insulating and nonferromagnetic, while the underneath SRO layers remain ferromagnetic (FM) and metallic (Figure 1). Namely, termination conversion triggers

an atomic-scale MIT confined within the SRO surface. This surface MIT can be fully understood by the surface-symmetry-breaking-induced electronic reconstructions at the RuO$_2$-terminated surface. This work illustrates how surface termination engineering provides a new path to manipulate the fundamental physical properties of TMO at atomic precision.

SRO thin films were grown on TiO$_2$-terminated SrTiO$_3$(001) [STO(001)] substrates via pulsed laser deposition.[24] The substrate temperature and oxygen partial pressure were optimized at 700 °C and 100 mTorr, respectively. By Combining the in situ reflection high energy electron diffraction (RHEED) monitoring and laser pulse counting, we can precisely control the SRO film thickness (t_{SRO}) at unit-cell scale precision (see the Experimental Section and Section S1 of the Supporting Information for procedural details). The epitaxial qualities of as-grown SRO films were confirmed by X-ray diffraction (Section S1, Supporting Information).

Realizing effective and uniform surface termination engineering is the first experimental challenge in this study. Previously reported termination engineering typically require in situ deposition of additional AO or BO_2 monolayers at uniformly terminated film surfaces.[26] However, during the high-temperature film deposition, complicated surface reconstructions easily occur due to the intricate energy landscape of the surface structures.[14,15,27,28] In addition, the high-energy growth kinetics facilitates mixtures of different surface terminations and unintended segregation of A-site cations.[29,30] These unwanted effects can easily hinder the atomic-precision control of the surface structure. Specifically, for the case of SRO films, the surface compound RuO$_2$ is highly volatile and unstable under the optimal growth condition.[23] Hence, the as-grown SRO film surface always exhibits a uniform SrO termination, and in situ growth of an additional RuO$_2$ monolayer on it should be extremely difficult. To overcome this challenge, we developed a room-temperature ex situ water-leaching method. Although bulk SRO is resistant to most acid etching processes,[18,31] the water solubilities of SrO and RuO$_2$ atomic layers at the film surface are distinct: SrO can react with H$_2$O molecular to produce water-soluble Sr(OH)$_2$, whereas RuO$_2$ cannot dissolve in water.[32] Therefore, the structure change of the as-grown SRO surface in water is expected to have a self-limiting nature. Based on this consideration, we ultrasonicated the as-grown SRO films in deionized water for various time durations (t_w) to trigger an unprecedented surface termination conversion from SrO to RuO$_2$. The procedural details are described in the Experimental Section.

We characterized the SRO film surface evolution during water-leaching via atomic force microscopy (AFM). After water-leaching the SRO film for various t_w, we acquired AFM height (**Figure 2**a–e) and phase (Figure 2f–j) images simultaneously. In addition to the topography, a variation in surface chemical composition can also influence sample-tip interaction, which makes the phase image a fingerprint of local variation in surface termination.[33,34] The detailed analysis of the correlation between surface termination and the AFM phase signal can be found in Section S2 of the Supporting Information. In Figure 2a, the height image of the as-grown sample ($t_w = 0$) shows an atomically flat surface with one-unit-cell-high terraces. The corresponding phase image (Figure 2f) shows negligible contrast except for the lines at terrace edges, indicating a uniform
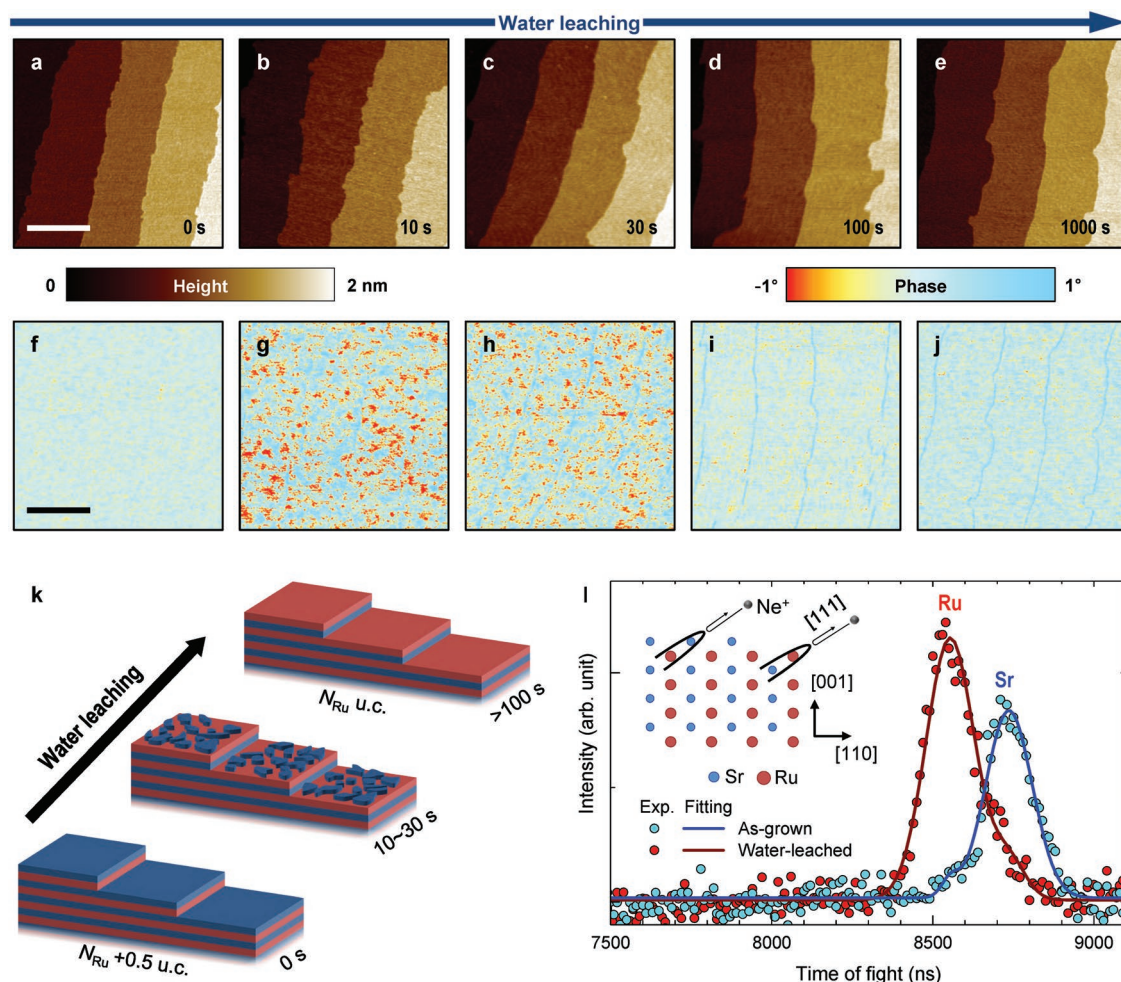
ADVANCED
SCIENCE NEWS
www.advancedsciencenews.com

ADVANCED
MATERIALS
www.advmat.de

Figure 2. SRO surface termination conversion triggered by water-leaching. a–j) Atomic force microscopy (AFM) topographic height images (a–e), and corresponding phase images (f–j) of the SRO thin film acquired after different water-leaching durations (t_w). The topographic height images do not show notable changes as t_w increases, while the phase images for t_w = 10 and 30 s exhibit clear inhomogeneous contrast, signifying the coexistence of SrO and RuO$_2$ surface terminations. All the scale bars correspond to 300 nm. k) Schematics of surface termination evolution during water-leaching. The topmost SrO layer is gradually dissolved during water leaching. The number of RuO$_2$ layers in SRO film is defined as N_{Ru}. Thicknesses (t_{SRO}) of SrO and RuO$_2$-terminated SRO films are N_{Ru} and N_{Ru} + 0.5 unit-cells (u.c.), respectively. l) Coaxial impact-collision ion scattering spectroscopy measurements on the as-grown (SrO-terminated, blue) and water-leached (RuO$_2$-terminated, red) SRO(001) surfaces. The experimental spectra (dotted lines) can be well fitted (solid lines) via two Gaussian peaks. The schematic inset illustrates the Ne$^+$ ion scattering process.

surface termination. After water-leaching for various t_w, the AFM height images (Figure 2b–e) do not show obvious changes in topography. By contrast, the phase images for t_w = 10 and 30 s become highly inhomogeneous (Figure 2g,h). The local phase difference exceeds 2°, signifying considerable variation in the surface chemical composition. By increasing t_w to 100 s, the phase image becomes uniform again (Figure 2i). It remains stable after additional leaching for t_w = 1000 s (Figure 2j). As shown in Section S3 of the Supporting Information, the surface and electronic transport of SRO films remained stable even after water-leaching for long-duration (48 h), which experimentally attests the self-limiting nature of the water-leaching process.

The evolution of the SRO film surface during water-leaching is schematically depicted in Figure 2k. The SrO surface layer is expected to react with water and gradually dissolve during the initial stage. After water-leaching for t_w = 10–30 s, the exposed

RuO$_2$ termination, remaining SrO termination, noncrystalline SrO$_x$ and Sr(OH)$_2$ residues should coexist. On the one hand, because of their superior sensitivity to surface chemical composition,[33] the AFM phase images become highly inhomogeneous. On the other hand, these SrO$_x$ or Sr(OH)$_2$ islands could be at nanoscale and thus may not make large contributions to the AFM height signal, instead only slightly increasing surface roughness (due to the limitation of AFM spatial resolution, see Section S2 of the Supporting Information for details). After water-leaching for t_w > 100 s, the SrO surface layer is completely removed. The resultant film surface is singly terminated by RuO$_2$. This compact and chemically stable atomic layer should remain unchanged and protect the films underneath during further water-leaching.

The surface termination conversion was further confirmed by coaxial impact-collision ion scattering spectroscopy (CAICISS).[35] CAICISS is a low-energy ion scattering spectroscopy, which
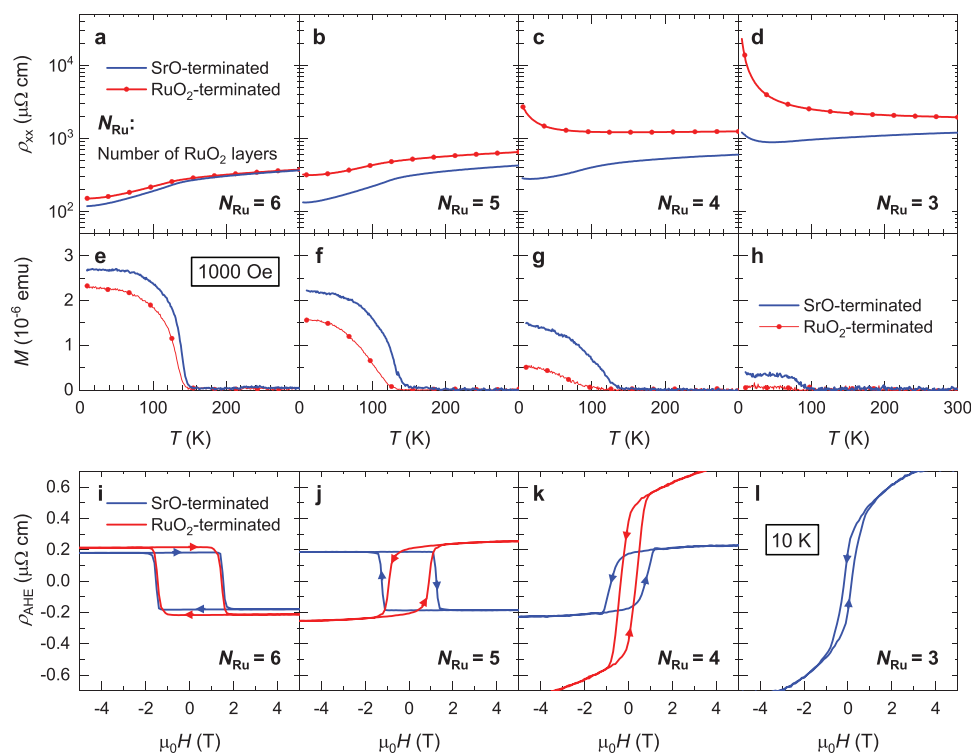
**ADVANCED
SCIENCE NEWS**

www.advancedsciencenews.com

**ADVANCED
MATERIALS**

www.advmat.de

Figure 3. Electrical transport and magnetic characterizations of SRO ultrathin films. a–h) Temperature-dependent longitudinal resistivity (a–d) and magnetization (e–h) (ρ_{xx}–T and M–T) curves of the SrO-terminated (blue curves) and RuO$_2$-terminated (red curves) SRO films with various N_{Ru}. The M–T curves are measured with an out-of-plane magnetic field (H) of 1000 Oe. i–l) H-dependent anomalous Hall resistivity (ρ_{AHE}–H) curves measured at 10 K from the SrO- and RuO$_2$-terminated SRO films with various N_{Ru}. All of the ordinary Hall components have been subtracted for clarity. The H scanning directions are indicated by solid arrows.

measures the time-of-flight (TOF) of injected ions backscattered by atoms at a crystal surface. The TOF profile depends largely on the masses of the surface atoms. As depicted in the inset of Figure 2l, when Ne$^+$ ions are injected along the [111] axis toward the SRO(001) surface, due to the atomic shadowing effect, only the topmost atoms can affect backscattering. In this case, the TOF profile is extremely sensitive to surface termination.[35] As shown in Figure 2l, the TOF profiles of the as-grown and water-leached SRO films show peaks with distinct positions (8736 and 8554 ns, respectively), which can be assigned to the backscattering processes from Sr and Ru atoms, respectively. According to the Gaussian fitting, the coverage of SrO termination for the as-grown sample is 96.9% ± 3.1% and the coverage of RuO$_2$ termination for the water-leached sample is 89.7% ± 3.0% (see the detailed analyses in Section S4, Supporting Information). These results further confirmed that both the as-grown and water-leached SRO films show nearly uniform surface terminations as expected.

Based on the uniformity in surface termination, we can define SRO film thickness (t_{SRO}) with sub-unit-cell accuracy. We denote the number of RuO$_2$ layers in the SRO film as N_{Ru}. The SrO-terminated SRO films grown on a TiO$_2$-terminated STO(001) substrate consist of N_{Ru}+1 SrO layers, while the RuO$_2$-terminated films consist of N_{Ru} SrO layers. Therefore, we denote the t_{SRO} of the SrO- and RuO$_2$-terminated SRO films as N_{Ru} + 0.5 and N_{Ru} u.c., respectively. X-ray reflection measurements (Section S1, Supporting Information) further confirm that water-leaching enables a sub-unit-cell control of t_{SRO}.

Surface termination conversion can strongly affect the longitudinal electrical transport and ferromagnetism of SRO ultrathin films. We measured the temperature-dependent longitudinal resistivity (ρ_{xx}–T, **Figure 3**a–d) and magnetization (M–T, Figure 3e–h) curves of the SRO films before and after water-leaching. Bulk SRO is a typical itinerant ferromagnet with Curie temperature (T_C) ≈ 160 K.[18] For the as-grown film with N_{Ru} = 6 (t_{SRO} = 6.5 u.c., SrO-terminated), the ρ_{xx}–T curve exhibits a bulk-like metallic behavior and a kink near T_C ≈ 145 K, where the corresponding M–T curve also shows a well-defined paramagnetic-FM transition. As N_{Ru} decreases from 6 to 3, the ρ_{xx}–T curve starts to show an insulating upturn at ≈47 K, and the T_C decreases from 145 to 99 K. The saturated M value also decreases significantly from 2.7×10^{-6} to 0.4×10^{-6} emu. Such clear decays in metallicity and ferromagnetism of the as-grown films are consistent with previous studies, which can be ambiguously understood in terms of spatial-confinement effect, reduced dimension, and phase transition to antiferromagnetic (AF) insulator.[36–38] After water-leaching, the RuO$_2$-terminated samples show a clear increase in ρ_{xx} and decrease in M. Such termination conversion-induced decays in both metallicity and ferromagnetism become more prominent as N_{Ru} decreases. Specifically, for the N_{Ru} = 4 case, the SrO-terminated sample remains metallic, while the RuO$_2$-terminated sample becomes highly insulating below 152 K. The N_{Ru} = 3 film with RuO$_2$-termination exhibits insulating behavior over the entire T range and a negligible FM signal. This behavior further implies that the RuO$_2$-termination may facilitate an AF insulating phase.[39]

**ADVANCED
SCIENCE NEWS**

www.advancedsciencenews.com

**ADVANCED
MATERIALS**

www.advmat.de

The termination conversion also significantly modulates the transverse magnetotransport properties. As an itinerant ferromagnet, SRO exhibits both ordinary and anomalous Hall effects (OHE and AHE, respectively). The Hall resistivity (ρ_{xy}) of SRO thin film can be described by $\rho_{xy} = \rho_{OHE} + \rho_{AHE}$.[40] The first term is the OHE resistivity $\rho_{OHE} = R_0 H$, where R_0 and H are the ordinary Hall coefficient and out-of-plane magnetic field, respectively. The second term is AHE resistivity $\rho_{AHE} = R_S M$, where R_S is the cumulative anomalous Hall coefficient. Figure 3i–l shows the ρ_{AHE}–H curves (at 10 K) of the SRO films before and after water-leaching. The linear OHE components are subtracted from all of the curves for clarity. For the as-grown sample (blue curve) with $N_{Ru} = 6$ ($t_{SRO} = 6.5$ u.c., SrO-terminated), ρ_{AHE}–H curves exhibit bulk-like AHE with negative R_S. As N_{Ru} decreases to 4 and 3, the sign of R_S changes from negative to positive. The AHE of SRO is dominated by the intrinsic Berry phase-related deflection.[22,40] Hence, this sign reversal can be understood in terms of the t_{SRO}-driven modulations in the Ru t_{2g} band structure and associated integral Berry curvature.[22,41] Note that intrinsic ρ_{AHE} is proportional to ρ_{xx}^2.[45] Therefore, the t_{SRO} reduction-induced decay in metallicity result in a dramatic increase of ρ_{AHE} for the $N_{Ru} = 3$ sample (Figure 3i). In addition, the coercive field of the $N_{Ru} = 3$ sample decreases due to the associated decay in ferromagnetism and magnetic domain size.[18] After water-leaching, R_S sign reversal occurs at $N_{Ru} = 5$, suggesting an effective modulation of band structure during the termination conversion. The ρ_{AHE} amplitude (coercive field) of the water-leached $N_{Ru} = 4$ sample increases (decreases) dramatically, further attesting the decay in both metallicity and ferromagnetism. We emphasize that both the line shape and amplitude of the ρ_{AHE}–H curves of the $N_{Ru} = 4$ and 5 water-leached samples look surprisingly similar to their as-grown counterparts with $N_{Ru} = 3$ and 4, respectively. Such similarity also can be identified in the line shapes of ρ_{xx}–T and M–T curves shown in Figure 3a–h. This universally observed similarity should imply a unique modulation of electrical/magnetic properties via surface termination conversion.

Furthermore, we analyzed the evolution of sheet resistivity (ρ_{sheet}), sheet carrier density (n_{sheet}), M (at 10 K), and T_c with t_{SRO}. As previously defined, for SrO-terminated (RuO$_2$-terminated) samples, the nominal $t_{SRO} = N_{Ru} + 0.5$ (N_{Ru}) u.c. As shown in **Figure 4**a–d, the t_{SRO}-dependent ρ_{sheet}, n_{sheet}, M, and T_c curves consistently exhibit a step-like line shape. Namely, the metallicity and ferromagnetism of the RuO$_2$-terminated SRO film consisting of N_{Ru} RuO$_2$ layers (i.e., $t_{SRO} = N_{Ru}$ u.c.) are nearly the same as those of the SrO-terminated film consisting of N_{Ru}-1 RuO$_2$ layers (i.e., $t_{SRO} = N_{Ru} - 0.5$ u.c.). Note that both the metallicity and ferromagnetism of SRO are dominated by its 3D RuO$_6$ octahedral networks. Accordingly, the topmost RuO$_2$ monolayer should not contribute to either electrical transport or ferromagnetism after water-leaching. In other words, even in an SRO film with robust bulk metallicity ($N_{Ru} \geq 5$), the RuO$_2$-terminated surface layer should become both insulating and non-FM. Moreover, the consistent step-like features shown in Figure 4a–d strongly suggest that the non-FM insulating state is strictly confined within the topmost SRO monolayer. Accordingly, the termination conversion triggers an atomic-scale surface MIT in our SRO ultrathin films.

The explicit link between surface metallicity and surface termination of SRO ultrathin film was verified by scanning tunneling spectroscopy (STS) measurements. Figure 4e,f shows the differential tunneling conductance versus bias (dI/dV–V) curves on the SrO- and RuO$_2$-terminated SRO surfaces, respectively. We obtain each curve by averaging 14 curves measured on clean and flat regions at 77 K (see the Experimental Section and Figure S4 of the Supporting Information for details). The dI/dV signal is proportional to the local density of states (DOS) at the surface.[9] The dI/dV–V curves of the SrO-terminated surface (Figure 4e) exhibit typical metallic characteristics: finite DOS at zero-bias and gradually increased DOS with bias. These features are also consistent with a previous report on the as-grown SRO surface.[42] By contrast, the dI/dV–V curves of the RuO$_2$-terminated surfaces (Figure 4f) clearly show a gap-like feature due to the negligible DOS near zero-bias. The average gap size is ≈0.30 eV. Note that the STS spectra of both SrO- and RuO$_2$-terminated surfaces exhibit considerable spatial variations (Section S5, Supporting Information), which can be ascribed to surface adsorbates arising from the unavoidable ex situ sample transfer procedure and water-leaching processes. In spite of this spatial variation, metallic (insulating) characteristics are consistently observed in all of the dI/dV–V curves from SrO-terminated (RuO$_2$-terminated) surfaces. Hence, the STS results quantitatively corroborate the surface MIT picture as depicted in Figure 1.

Water-leaching-induced self-limiting termination conversion is technically essential for research on ultrathin oxide films. Taking SrO-terminated SRO ultrathin film as an example, the surface termination conversion can be triggered by very short-duration water-leaching (≈30 s). Therefore, it could occur during water-solution-based nanofabrication procedures, or even with simple storage in a humid atmosphere (Section S1, Supporting Information). An unexpected surface termination conversion of this type could cause considerable changes in the magnetism and electrical transport of ultrathin oxide films. On the contrary, the RuO$_2$-terminated SRO ultrathin films can be quite stable against humidity and long-duration water leaching (Section S3, Supporting Information). On this basis, we suggest that these differences and nonuniformity of surface termination could be an important factor to cause a large deviation from previously reported electric/magnetic critical thickness values in SRO ultrathin films.[36,43] For investigating the electrocatalytic activity of SRO,[44,45] the stability of surface termination in water-based solutions should also be seriously considered.

We now turn to explore the underlying mechanism of MIT triggered by surface termination conversion. We first excluded the extrinsic effects from surface adsorbates by measuring ρ_{xx} – T curves during high-temperature vacuum annealing (Section S3, Supporting Information). Furthermore, as both SrO- and RuO$_2$-terminated SRO(001) surfaces are nonpolar in nature, we expect surface polarity-induced surface lattice distortion to be minimal, and thus to have little impact on the surface MIT.[17] The room temperature water-leaching process might not trigger complicated surface reconstructions at the RuO$_2$-terminated surface.[14,15,27,28] On this basis, we suggest that the loss of apex oxygen at the RuO$_2$-terminated surface locally breaks the RuO$_6$ octahedral symmetry and associated crystal fields, thus leading to significant changes in both electronic and magnetic structures.[46,47]
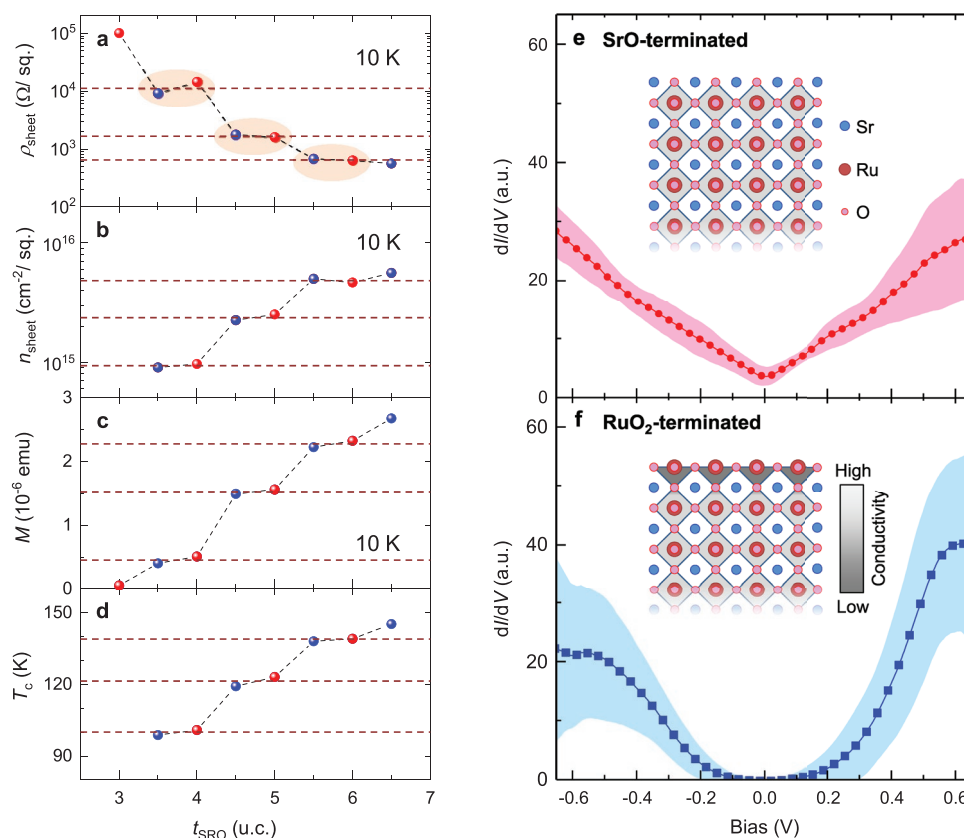
Figure 4. Evolution of electrical transport and magnetic properties with t_{SRO} and surface termination. a–d) t_{SRO}-dependent sheet resistivity (ρ_{sheet}) (a), sheet carrier density (n_{sheet}) (b), M (c), and Curie temperature (T_C) (d) of the SRO thin films. The ρ_{sheet}, n_{sheet}, and M values were measured at 10 K. All curves exhibit a step-like feature, signifying that the metallicity and magnetism of RuO$_2$-terminated samples consisting of N_{Ru} RuO$_2$ layers are similar to those of SrO-terminated samples consisting of N_{Ru}-1 RuO$_2$ layers. e,f) Scanning tunneling spectroscopies of the SrO-terminated (e) and RuO$_2$-terminated (f) samples. The solid lines are bias-dependent differential conductance (dI/dV–V) curves averaged from 14 curves measured at flat and clean surface regions (Figure S4, Supporting Information). The colored backgrounds indicate the standard deviations. The dI/dV–V curves from the SrO-terminated surface show typical metallic characteristics while the curves from the RuO$_2$-terminated surface show well-defined energy gaps. The insets of (e) and (f) are schematic atomic structures of SRO films with SrO- and RuO$_2$-terminated surfaces, respectively. The electrical conductivity of the topmost SRO monolayer with RuO$_2$-termination decays significantly.

To obtain a theoretical basis of the surface symmetry-breaking scenario, we performed density functional theory (DFT) calculations on the termination-dependent electronic structure and spin configuration. We constructed SrO- and RuO$_2$-terminated SRO/STO(001) films, stacked with a 15 Å thick vacuum layer (see the Experimental Section for details). We set the N_{Ru} = 5, which is well above the previously predicted critical value for triggering any phase transition to the insulating and non-FM state.[39] For the SrO-terminated SRO/STO(001) film, the DOS projected along all the RuO$_2$ layers exhibits typical metallic characteristics (Section S6, Supporting Information), similar to that of bulk SRO. By contrast, for the RuO$_2$-terminated SRO film, the surface RuO$_2$ layer exhibits almost no DOS near E_F, while the other RuO$_2$ layers underneath show bulk-like metallic DOS profiles (Section S6, Supporting Information).

As shown schematically in Figure 1a, the Ru^{4+} cations inside the bulk SRO are under an octahedral crystal field. This crystal field splits Ru 4d orbitals into triply degenerate t_{2g} (d$_{xy}$, d$_{yz}$, and d$_{xz}$) orbitals and doubly degenerate e_g (d$_{x^2-y^2}$ and d$_{3z^2-r^2}$) orbitals. **Figure 5**a shows the orbital-resolved DOS profiles projected along a RuO$_2$ layer inside RuO$_2$-terminated SRO film.

Because of the high energy difference between the t_{2g} and e_g orbitals, the four Ru 4d electrons occupy t_{2g} orbitals only: three of them occupy the spin-majority channel and the remaining one occupies the minority channel, leading to a low spin configuration.[47] Similar orbital occupancy can be found in the other RuO$_2$ layers underneath the surface layer and in SrO-terminated SRO film.

As schematically depicted in Figure 1b, the Ru^{4+} cations at the RuO$_2$-terminated surface layer, by contrast, are under a unique square pyramidal crystal field. This crystal field with lower symmetry further degenerates the t_{2g} and e_g orbitals. The orbital-resolved DOS profiles projected along the RuO$_2$ surface layer are shown in Figure 5b. The d$_{3z^2-r^2}$ orbital states shift downward dramatically below E_F, thus leading to the gap opening. The gap size is ≈0.25 eV, close to the value derived from STS measurements. Moreover, the four Ru 4d electrons occupy three t_{2g} orbitals as well as one e_g (d$_{3z^2-r^2}$) orbital in the spin majority channel, leading to a high spin configuration. We also tested several possible magnetic orderings in the RuO$_2$-terminated SRO film and found the energetically favorable magnetic ground state is bulk FM with surface G-type AF
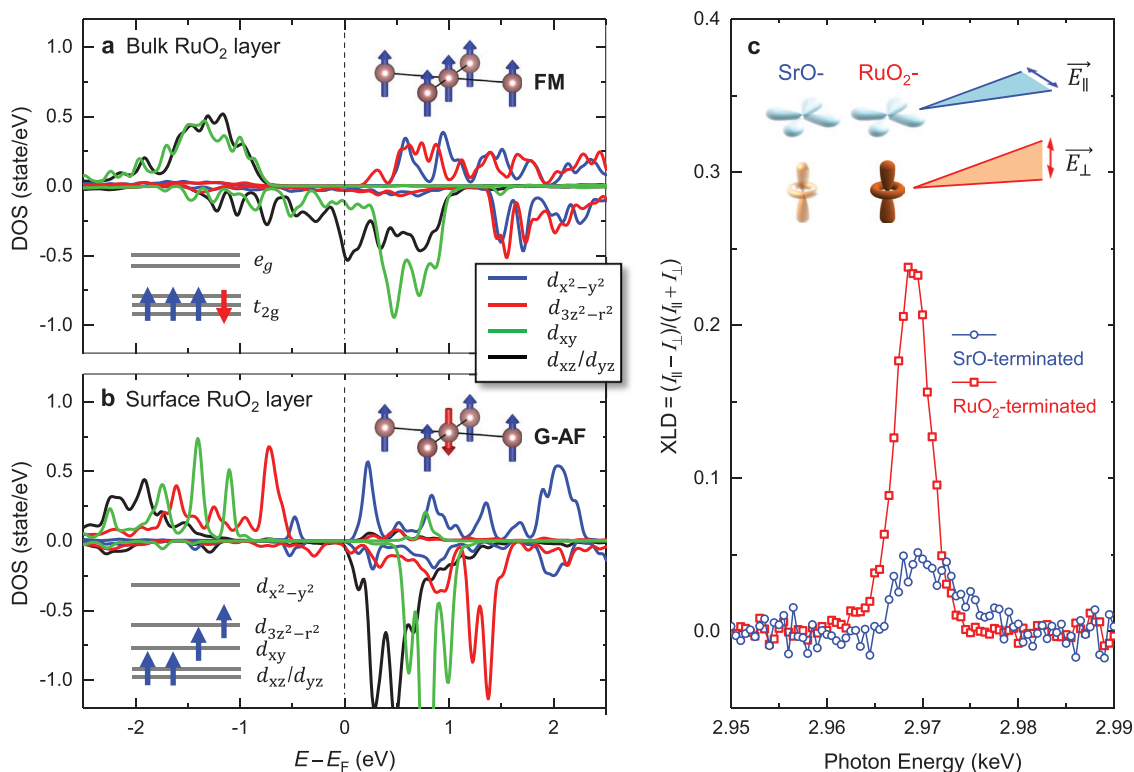
Figure 5. Electronic structure and 4d orbital occupancy in SRO ultrathin film. a) Orbital-resolved DOS projected along the third RuO₂ layer inside RuO₂-terminated SRO film (denoted as the bulk RuO₂ layer). b) Orbital-resolved DOS projected along the RuO₂-terminated surface layer. The bulk RuO₂ layer exhibits finite DOS near the E_F, signifying typical metallic characteristics. On the contrary, the surface RuO₂ layer shows almost zero DOS near the E_F, giving rise to insulating characteristics. The gap size is ≈0.25 eV. Insets of (a) and (b) illustrate the low-spin ferromagnetic (FM) and high-spin G-type antiferromagnetic (G-AF) configurations in the bulk and surface RuO₂ layers, respectively. c) X-ray linear dichroism (XLD) at the Ru L_2 edge measured from the SrO- and RuO₂-terminated SRO films ($N_{Ru} = 5$). $I_{\parallel}$ and $I_{\perp}$ are X-ray absorption spectroscopy intensities with linear light polarization parallel ($E_{\parallel}$) and perpendicular ($E_{\perp}$) to the (001) surface. The schematic inset shows how the $d_{x^2-y^2}$ (top) and $d_{3z^2-r^2}$ (bottom) orbitals couple with the incident linear-polarized X-ray. The light-color (deep-color) indicates the unoccupied (occupied) orbitals.

(Section S6, Supporting Information). This spin configuration is ≈60 meV lower in energy compared to the pure FM configuration.

The surface-termination-controlled 4d orbital occupancy can be further verified by the X-ray linear dichroism (XLD). We performed X-ray absorption spectroscopy (XAS) measurements on the SrO- and RuO₂-terminated SRO films ($N_{Ru} = 5$) at the Ru L_2-edge with the linear light polarization perpendicular ($E_{\perp}$) and parallel ($E_{\parallel}$) to the film surface. The corresponding XAS intensities $I_{\perp}$ and $I_{\parallel}$ are dominated by the unoccupied $d_{3z^2-r^2}$ and $d_{x^2-y^2}$ orbitals, respectively.[46] The XLD is calculated as the normalized XAS intensity difference $(I_{\perp} - I_{\parallel})/(I_{\perp} + I_{\parallel})$. As shown in Figure 5c, the RuO₂-terminated SRO film shows a positive XLD peak, signifying a preferential electron occupation in the $d_{3z^2-r^2}$ orbital. By contrast, the SrO-terminated SRO film shows a much weaker XLD peak. Since both e_g orbitals are unoccupied, this weak XLD signal may arise from compressive strain induced slight preferential electron occupancies in the d_{xz} and d_{yz} orbitals. The consistency between the DFT and XLD results confirms that the surface termination-controlled Ru 4d orbital occupancy can comprehensively explain the non-FM insulating state at the RuO₂-terminated SRO surface.

In summary, we discovered an atomic-scale MIT at the SRO ultrathin film surface. An ex situ water-leaching method was

developed for effective and uniform surface termination engineering in SRO. As the surface termination converts from SrO to RuO₂, the topmost SRO atomic layer undergoes an MIT while the atomic layers underneath remain metallic. We can fully understand this MIT according to the surface symmetry breaking-induced changes in the 4d orbital occupancies and electronic structures. This surface MIT may be accompanied by significant modulations of other physical properties in the atomic scale, such as the emergence of surface AF ordering with a high-spin configuration. The self-limiting water-leaching recipe can be easily generalized to other TMO-based epitaxial systems for surface termination engineering. Therefore, our finding paves a promising route toward triggering and tuning exotic physical phenomena with atomic precision. The resultant intriguing functionalities are expected to be spatially confined near the surfaces or heterointerfaces, which also imply possible integration and coupling with emergent phenomena in other low-dimensional electronic systems.

Experimental Section

Film Deposition: SRO thin films were deposited onto STO(001) substrates using pulsed laser deposition. The as-received STO(001) substrates (Crystec) were treated with buffered hydrofluoric acid and

annealed in the ambient atmosphere to achieve an atomically flat and TiO$_2$-terminated surface with one-unit-cell-high terraces. The SRO ultrathin films were grown under an oxygen partial pressure of 100 mTorr. The substrate temperature was maintained at 700 °C during the deposition. An SRO polycrystalline target was ablated by a KrF excimer laser (λ = 248 nm; Coherent) with a laser fluence of $\approx$2 J cm^{-2}. The growth rate of the film was calculated according to the RHEED oscillations of the initial 2.5 u.c growth divided by the number of laser pulses. After the initial 2.5 u.c. growth, the growth mode of the film transited from layer-by-layer to step-flow. The t_{SRO} was precisely controlled by using the growth rate calculated from the layer-by-layer growth mode regime (Section S1, Supporting Information).

Termination Engineering via *Water-Leaching*: As-grown SRO films were cut into two pieces, one for water-leaching and one serving as an as-grown reference. The as-grown sample was dipped in the deionized water and ultrasonicated it for various time duration t_w. After water-leaching, the sample was sequentially rinsed with ethanol, acetone, and isopropanol to remove the surface residues and contaminations. The rinsing processes were repeated for 3 cycles. The sample was then dried at 150 °C in ambient for 30 min.

Surface Structure Characterizations: The AFM measurements were performed at room temperature using a scanning probe microscope (Cypher, Asylum Research) with a commercial AFM tip (Tap300Al-G; Budget Sensors). The spring constant, resonance frequency, and radius of the AFM tips were $\approx$40 N m^{-1}, $\approx$300 kHz, and $\approx$10 nm, respectively. The tapping mode was used to acquire topographic height and phase images simultaneously. CAICISS measurement was performed using a 3 keV Ne source in a high vacuum chamber ($<1 \times 10^{-6}$ Torr) at room temperature. The Ne$^+$ beam was aligned along the STO[111] crystallographic orientation. In this incident direction, the Ne$^+$ ions can be backscattered by the surface atoms only. The STO[111] axes were identified by azimuthal and surface-normal polar angle scan of the backscattering intensity.

Magnetization and Electrical Transport Measurement: The *M*–*T* curves were measured using a SQUID magnetometer (MPMS; Quantum Design) with an external magnetic field of 0.1 T applied along the out-of-plane direction. The longitudinal and transverse transport data were measured using a physical properties measurement system (PPMS; Quantum Design). Pt/Ti electrodes with 6-probe Hall bar geometry were sputtered onto the SRO films.

Scanning Tunneling Microscopy and Spectroscopy: Scanning tunneling microscopy (STM) and STS measurements were performed at 77 K in an ultrahigh vacuum chamber ($<2 \times 10^{-10}$ Torr; Scienta-Omicron) interfaced to Nanois controller (SPECS Zurich). Electrochemically etched tungsten tips were used, and external voltage bias was applied to the sample electrode. For the STM measurements, the constant current mode was adopted and the tunneling current was in the range of 200–1000 pA. For the STS measurements, the lock-in technique was used to record the tunneling current, with a modulation voltage of 30 mV and a frequency of 963 Hz. Before the STM and STS measurements, the samples were degassed to 150 °C for 60 min in the ultrahigh vacuum chamber.

DFT Calculations: A five-layer SRO thin film was constructed on an STO(001) substrate, including a 15 Å thick vacuum layer stacked on the SRO surface. DFT calculations on four-layer SRO thin film were also performed and the results are qualitatively consistent with those obtained from five-layer SRO thin film. The in-plane lattice constant was fixed at 3.905 Å (the experimental value of cubic STO). The atomic structure was calculated using the Vienna Ab initio Simulation Package (VASP) with GGA–PBE functional.[48–50] The cut-off energy was set as 500 eV and the Brillouin zone was sampled with a $9 \times 9 \times 1$ *k*-mesh. To better describe the correlation effects of the d electrons in TMOs, the Dudarev's rotationally invariant GGA+U approach was used,[51] taking U = 3.0 eV for Ru and 5.0 eV for Ti. For the RuO$_2$-terminated SRO film, the most energetically favorable solution was determined by testing various magnetic structures (FM or AF) and spin configurations (high-spin or low-spin). The details can be found inSection S6 of the Supporting Information.

XLD Measurements: XLD measurements were performed at the materials and magnetism beamline, I16 at the Diamond Light Source (Didcot, UK).[52] XAS was first measured at the Ru L$_2$ absorption edge (2.967 keV) using the fluorescence-yield mode. The linear polarization of photons was set to be parallel or perpendicular to the film surface. The background scattering signals were fitted using $y = a \cdot \tan^{-1}x + bx + c$ functions, and subtracted them from the raw data. After background subtracting, the XAS intensities with the two orthogonal linear polarizations ($I_\perp$ and $I_\parallel$) were normalized according to the footprints of the beam profiles, to avoid any artificial signal in XLD. The XLD is calculated as the normalized differences in XAS signals $(I_\perp - I_\parallel)/(I_\perp + I_\parallel)$. All the spectra were recorded at 300 K. The ultrathin SRO films were chosen to measure with N_{Ru} = 5, in which the orbital occupancy changes occurred at surface monolayer still can give a large enough spectral weight for detection.

Supporting Information

Supporting Information is available from the Wiley Online Library or from the author.

Conflict of Interest

The authors declare no conflict of interest.

**ADVANCED
SCIENCE NEWS**

www.advancedsciencenews.com

**ADVANCED
MATERIALS**

www.advmat.de

[1] M. Imada, A. Fujimori, Y. Tokura, *Rev. Mod. Phys.* **1998**, *70*, 1039.

[2] S. Y. Kim, M.-C. Lee, G. Han, M. Kratochvilova, S. Yun, S. J. Moon, C. Sohn, J.-G. Park, C. Kim, T. W. Noh, *Adv. Mater.* **2018**, *30*, 1704777.

[3] M. M. Qazilbash, M. Brehm, B.-G. Chae, P.-C. Ho, G. O. Andreev, B.-J. Kim, S. J. Yun, A. V. Balatsky, M. B. Maple, F. Keilmann, H.-T. Kim, D. N. Basov, *Science* **2007**, *318*, 1750.

[4] H. Kuwahara, Y. Tomioka, A. Asamitsu, Y. Moritomo, Y. Tokura, *Science* **1995**, *270*, 961.

[5] B. J. Kim, H. Jin, S. J. Moon, J.-Y. Kim, B.-G. Park, C. S. Leem, J. Yu, T. W. Noh, C. Kim, S.-J. Oh, J.-H. Park, V. Durairaj, G. Cao, E. Rotenberg, *Phys. Rev. Lett.* **2008**, *101*, 076402.

[6] R. Waser, M. Aono, *Nat. Mater.* **2007**, *6*, 833.

[7] Z. Yang, C. Ko, S. Ramanathan, *Annu. Rev. Mater. Res.* **2011**, *41*, 337.

[8] M. Basletic, J.-L. Maurice, C. Carretero, G. Harranz, O. Copie, M. Bibes, E. Jacquet, K. Bouzehouane, S. Fusil, A. Barthelemy, *Nat. Mater.* **2008**, *7*, 621.

[9] R. G. Moore, J. Zhang, V. B. Nascimento, R. Jin, J. Guo, G. T. Wang, Z. Fang, D. Mandrus, E. W. Plummer, *Science* **2007**, *318*, 615.

[10] P. Sharma, Q. Zhang, D. Sando, C. H. Lei, Y. Liu, J. Li, V. Nagarajan, J. Seidal, *Sci. Adv.* **2017**, *3*, e1700512.

[11] C. Cen, S. Thiel, G. Hammerl, C. W. Schneider, K. E. Andersen, C. S. Hellberg, J. Mannhart, J. Levy, *Nat. Mater.* **2008**, *7*, 298.

[12] S. Lee, K. Hippalgaonkar, F. Yang, J. Hong, C. Ko, J. Suh, K. Liu, K. Wang, J. J. Urban, X. Zhang, C. Dames, S. A. Hartnoll, O. Delaire, J. Wu, *Science* **2017**, *355*, 371.

[13] T. Kimura, Y. Tokura, *Annu. Rev. Mater. Sci.* **2000**, *30*, 451.

[14] J. Shin, A. Y. Borisevich, V. Meunier, J. Zhou, E. W. Plummer, S. V. Kalinin, A. P. Baddorf, *ACS Nano* **2010**, *4*, 4190.

[15] T. Kubo, H. Nozoye, *Surf. Sci.* **2003**, *542*, 177.

[16] L. Wang, R. Kim, Y. Kim, C. H. Kim, S. Hwang, M. R. Cho, Y. J. Shin, S. Das, J. R. Kim, S. V. Kalinin, M. Kim, S. M. Yang, T. W. Noh, *Adv. Mater.* **2017**, *29*, 1702001.

[17] D. P. Kumah, A. Malashevich, A. S. Disa, D. A. Arena, F. J. Walker, S. Ismail-Beigi, C. H. Ahn, *Phys. Rev. Appl.* **2014**, *2*, 054004.

[18] G. Koster, L. Klein, W. Siemons, G. Rijnders, J. S. Dodge, C.-B. Eom, D. H. A. Blank, M. R. Beasley, *Rev. Mod. Phys.* **2012**, *84*, 253.

[19] Y. J. Shin, Y. Kim, S.-J. Kang, H.-H. Nahm, P. Murugavel, J. R. Kim, M. R. Cho, L. Wang, S. M. Yang, J.-G. Yoon, J.-S. Chung, M. Kim, H. Zhou, S. H. Chang, T. W. Noh, *Adv. Mater.* **2017**, *29*, 1602795.

[20] P. B. Allen, H. Berger, O. Chauvet, L. Forro, T. Jarlborg, A. Junod, B. Revaz, G. Santi, *Phys. Rev. B* **1996**, *53*, 4393.

[21] L. Klein, J. S. Dodge, C. H. Ahn, G. J. Snyder, T. H. Geballe, M. R. Beasley, A. Kapitulnik, *Phys. Rev. Lett.* **1996**, *77*, 2774.

[22] Z. Fang, N. Nagaosa, K. S. Takahashi, A. Asamitsu, R. Mathieu, T. Ogasawara, H. Yamada, M. Kawasaki, Y. Tokura, K. Terakura, *Science* **2003**, *302*, 92.

[23] Y. Ohuchi, J. Matsuno, N. Ogawa, Y. Kozuka, M. Uchida, Y. Tokura, M. Kawasaki, *Nat. Commun.* **2018**, *9*, 213.

[24] L. Wang, Q. Feng, Y. Kim, R. Kim, K. H. Lee, S. D. Pollard, Y. J. Shin, H. Zhou, W. Peng, D. Lee, W. Meng, H. Yang, J. H. Han, M. Kim, Q. Lu, T. W. Noh, *Nat. Mater.* **2018**, *17*, 1087.

[25] G. Rijnders, D. H. A. Blank, J. Choi, C. B. Eom, *Appl. Phys. Lett.* **2004**, *84*, 505.

[26] R. Takahashi, Y. Matsumoto, T. Ohsawa, M. Lippmaa, M. Kawasaki, H. Koinuma, *J. Cryst. Growth* **2002**, *234*, 505.

[27] J. M. P. Martirez, E. H. Morales, W. A. Saidi, D. A. Bonnell, A. M. Rappe, *Phys. Rev. Lett.* **2012**, *109*, 256802.

[28] Y. J. Shin, L. Wang, Y. Kim, H.-H. Nahm, D. Lee, J. R. Kim, S. M. Yang, J.-G. Yoon, J.-S. Chung, M. Kim, S. H. Chang, T. W. Noh, *Appl. Mater. Interfaces* **2017**, *9*, 23305.

[29] H. Y. Sun, Z. W. Mao, T. W. Zhang, L. Han, T. T. Zhang, X. B. Cai, X. Guo, Y. F. Li, Y. P. Zang, W. Guo, J. H. Song, D. X. Ji, C. Y. Gu, C. Tang, Z. B. Gu, N. Wang, Y. Zhu, D. G. Schlom, Y. F. Nie, X. Q. Pan, *Nat. Commun.* **2018**, *9*, 2965.

[30] W. Jung, H. L. Tuller, *Energy Environ. Sci.* **2012**, *5*, 5370.

[31] D. M. Paskiewicz, R. Sichel-Tissot, E. Karapetrova, L. Stan, D. D. Fong, *Nano Lett.* **2016**, *16*, 534.

[32] W. M. Haynes, D. R. Lide, T. J. Bruno, *CRC Handbook of Chemistry and Physics*, CRC Press, Boca Raton, FL, USA **2014**.

[33] R. García, R. Magerle, R. Perez, *Nat. Mater.* **2007**, *6*, 405.

[34] R. Bachelet, F. Sanchez, F. J. Palomares, C. Ocal, J. Foncuberta, *Appl. Phys. Lett.* **2009**, *95*, 141915.

[35] M. Yoshimoto, T. Maeda, K. Shimozono, H. Koinuma, M. Shinohara, O. Ishiyama, F. Ohtani, *Appl. Phys. Lett.* **1994**, *65*, 3197.

[36] Y. J. Chang, C. H. Kim, S.-H. Phark, Y. S. Kim, J. Yu, T. W. Noh, *Phys. Rev. Lett.* **2009**, *103*, 057201.

[37] J. Xia, W. Siemons, G. Koster, M. R. Beasley, A. Kapitulnik, *Phys. Rev. B* **2009**, *79*, 140407.

[38] K. Ishigami, K. Yoshimatsu, D. Toyota, M. Takizawa, T. Yoshida, G. Shibata, T. Harano, Y. Takahashi, T. Kadono, V. K. Verma, V. R. Singh, Y. Takeda, T. Okane, Y. Saitoh, H. Yamagami, T. Koide, M. Oshima, H. Kumigashira, A. Fujimori, *Phys. Rev. B* **2015**, *92*, 064402.

[39] L. Si, Z. Zhong, J. M. Tomczak, K. Held, *Phys. Rev. B* **2015**, *92*, 041108.

[40] N. Nagaosa, J. Sinova, S. Onoda, A. H. MacDonald, N. P. Ong, *Rev. Mod. Phys.* **2010**, *82*, 1539.

[41] L. Wang, Q. Feng, H. G. Lee, E. K. Ko, Q. Lu, T. W. Noh, arXiv:1908.08211 [cond-mat.mtrl-sci], **2019**.

[42] I. Asulin, O. Yuli, G. Koren, O. Millo, *Phys. Rev. B* **2006**, *74*, 009501.

[43] H. Boschker, T. Harada, T. Asaba, R. Ashoori, A. V. Boris, H. Hilgenkamp, C. R. Hughes, M. E. Holtz, L. Li, D. A. Muller, H. Nair, P. Reith, X. R. Wang, D. G. Schlom, A. Soukiassian, J. Mannhart, *Phys. Rev. X* **2019**, *9*, 011027.

[44] S. H. Chang, N. Danilovic, K.-C. Chang, R. Subbaraman, A. P. Paulikas, D. D. Fong, M. J. Highland, P. M. Baldo, V. R. Stamenkovic, J. W. Freeland, J. A. Eastman, N. M. Markovic, *Nat. Commun.* **2014**, *5*, 4191.

[45] S. A. Lee, S. Oh, J.-Y. Hwang, M. Choi, C. Youn, J. W. Kim, S. H. Chang, S. Woo, J.-S. Bae, S. Park, Y.-M. Kim, S. Lee, T. Choi, S. W. Kim, W. S. Choi, *Energy Environ. Sci.* **2017**, *10*, 924.

[46] D. Pesquera, G. Herranz, A. Barla, E. Pellegrin, E. Magnano, F. Sánchez, J. Fontcuberta, *Nat. Commun.* **2012**, *3*, 1189.

[47] P. Mahadevan, F. Aryasetiawan, A. Janotti, T. Sasaki, *Phys. Rev. B* **2009**, *80*, 035106.

[48] G. Kresse, J. Hafner, *Phys. Rev. B* **1993**, *47*, 558.

[49] G. Kresse, J. Furthmüller, *Phys. Rev. B* **1996**, *54*, 11169.

[50] J. P. Perdew, K. Burke, M. Ernzerhof, *Phys. Rev. Lett.* **1996**, *77*, 3865.

[51] S. L. Dudarev, G. A. Botton, S. Y. Savrasov, C. J. Humphreys, A. P. Sutton, *Phys. Rev. B* **1998**, *57*, 1505.

[52] D. G. Porter, V. Granata, F. Forte, S. D. Matteo, M. Cuoco, R. Fittipaldi, A. Vecchione, A. Bombardi, *Phys. Rev. B* **2018**, *98*, 125142.